ACS APPLIED MATERIALS & INTERFACES

www.acsami.org

Research Article

Spatiotemporal Control of Melanin Synthesis in Liquid Droplets

Tlalit Massarano, Avigail Baruch Leshem, Michal Weitman, and Ayala Lampel*

Cite This: *ACS Appl. Mater. Interfaces* 2022, 14, 20520−20527

Read Online

ACCESS | Metrics & More | Article Recommendations | Supporting Information

ABSTRACT: Melanins are natural biopolymers that have remarkable properties including UV-protection, coloration, and antioxidant activity. Their biosynthesis is regulated both spatially and temporally and involves supramolecular templating and compartmentalization of enzymes and reactants within specialized organelles called melanosomes. In contrast, the laboratory-based bulk synthesis of melanin by tyrosine or dopamine oxidation is a poorly controlled process, resulting in materials with undefined properties. Inspired by the pigment's biosynthesis, we developed a methodology to spatiotemporally regulate melanin formation in liquid droplets. The spatial control is achieved by sequestration of the reaction in dextran-rich droplets of a polyethylene glycol/dextran aqueous two-phase system, where the use of a photocleavable protected tyrosine provides a temporal control over its enzymatic oxidation−polymerization. We show that the liquid droplets allow for confined local reactivity as they serve as reaction centers for melanin synthesis and compartmentalize the melanin product. This methodology opens tremendous opportunities for applications in skincare and biomedicine.

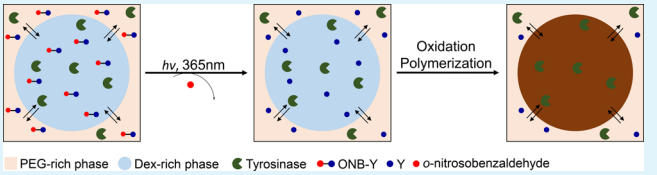

KEYWORDS: *bioinspired materials, liquid droplets, phase separation, melanin, reaction compartmentalization, spatiotemporal control*

INTRODUCTION

Living cells are spatiotemporally ordered systems, in which (bio)chemical reactions are regulated by microcompartmentalization in subcellular membrane-bound or membraneless organelles.[1] This spatiotemporal control is demonstrated by the biosynthesis of melanin pigments.[2,3] Melanins are a group of biopolymers with unique physicochemical properties which are found throughout nature, where they serve various functionalities, including UV-protection, coloration, and free radical scavenging.[4] Human and animal melanins are produced in specialized organelles called melanosomes, which mature across four morphologically distinct stages.[2] Stages I and II are characterized by proteinaceous fibrils that are formed by the functional amyloid protein Pmel17.[5] Melanin synthesis occurs during stages III and IV, where tyrosine (Y) molecules, oxidized by the enzyme tyrosinase, are deposited on the pre-assembled fibrils and subsequently polymerize to form the mature spherical or ellipsoidal melanosome.[2,3] In contrast to this highly regulated synthesis, the laboratory-based bulk synthesis of melanins is a poorly controlled process, resulting in insoluble material with undefined molecular composition and limited potential in technological applications.

These challenges have inspired extensive efforts to design synthetic mimics of melanin and melanin-like materials[6−8] for applications in structural colorations,[9−11] photoprotection, and free-radical scavenging,[12,13] including melanosome mimics,[14] and other photonic applications.[15] Most of these mimetic materials are based on polydopamine (PDA) synthesis by autoxidation of dopamine into spherical aggregates,[16,17] which absorb intensely in the UVB-UVA region, or synthetic melanin particles formed by ceramic templating, which enables a control of particle size and morphology.[18,19] While their properties resemble those of natural melanins, the synthesis of PDA-based mimetic materials typically requires high pH[12,20] and cannot be spatially regulated, and the templated approach does not allow a temporal regulation of melanin synthesis. Thus, there is still a vast gap in understanding and mimicking the biological manufacturing process of melanins and in controlling their synthesis and chemical/structural properties.

Membraneless organelles are liquid-like assemblies which actively form and dissolve in a stimuli-responsive manner by liquid−liquid phase separation (LLPS) of biomolecules.[21−23] LLPS is a common phenomenon in polymer chemistry, and is typically formed by associative or non-associative (segregative) separation of aqueous polymer solutions.[24] Associative LLPS, or coacervation, results in a macromolecule-dense phase (coacervate) along with a dilute phase, and is related to intracellular membraneless organelles.[21,23] Segregative phase separation is classically composed of two neutral polymers, or a polymer and a salt, creating different regions, each enriched in one of the components, and known as an aqueous two-phase system (ATPS).[24] Both forms of LLPS microdroplets have been used as synthetic models of protocells.[21,24] In particular, ATPS, based on polyethylene glycol (PEG) and dextran (Dex), have been extensively studied in bulk and within lipid

Received: October 31, 2021
Accepted: April 5, 2022
Published: April 22, 2022

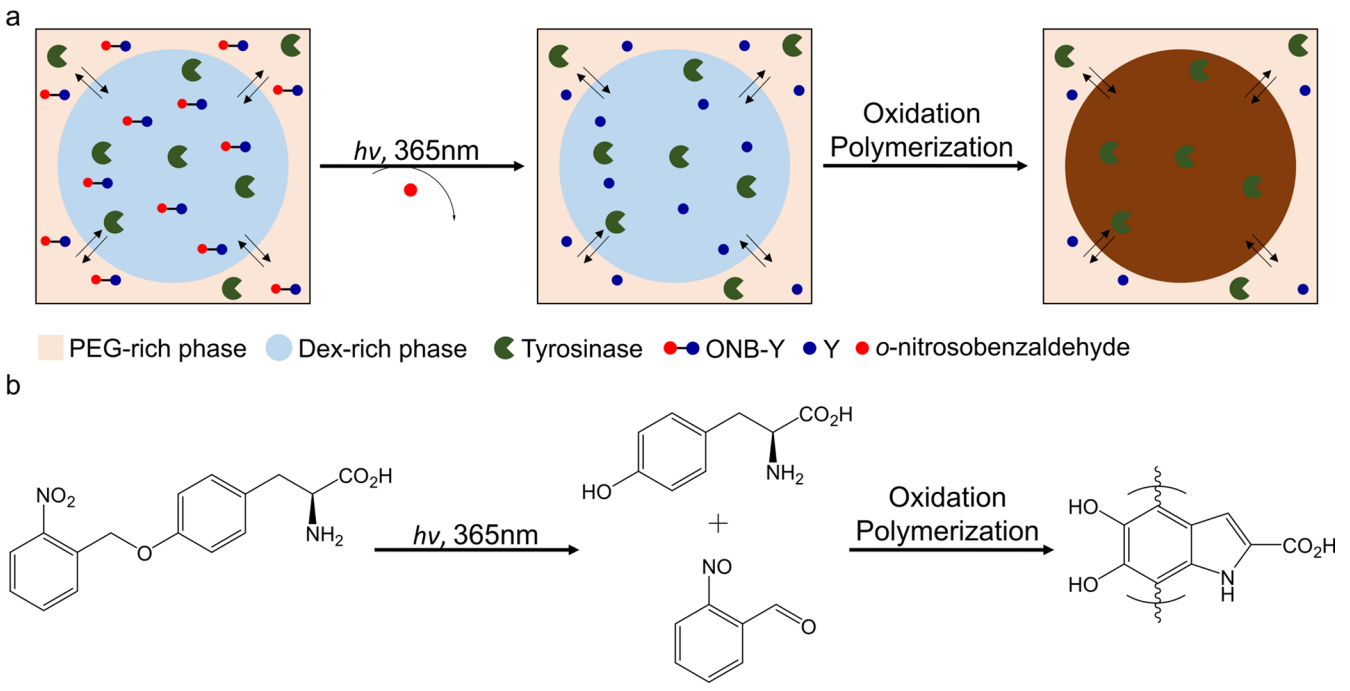

Figure 1. Controlling melanin synthesis in liquid droplets. (a) A schematic illustration of PEG/Dex ATPS for the sequestration of ONB-Y and tyrosinase. The photocleavable ONB group is removed with UV irradiation, enabling the oxidation-polymerization of the free Y within the droplets, resulting in a color change of the reaction mixture to dark brown. The cleaved *o*-nitrosobenzaldehyde may be involved in the melanin polymerization. (b) Chemical structures and reaction of ONB-Y cleavage under UV irradiation, followed by enzymatic oxidation-polymerization of the free Y.

vesicles.[24] The PEG/Dex microdroplets provide macromolecularly crowded open compartments which mimic the cell milieu,[24] where molecules can reversibly diffuse between the phases, thus can serve as microreactors for the control of biochemical reactions.[25,26] The partitioning of different solutes such as proteins and small molecules into one of the phases provide a means for controlling localized reactivity by compartmentalization.[25]

Here, we developed a methodology to spatiotemporally control melanin synthesis in dynamic melanosome-inspired PEG/Dex protocells. In this system, the Dex-rich droplets of the PEG/Dex ATPS serve as liquid compartments, allowing the synthesis to occur in a confined space, similar to melanins' spatially controlled biosynthesis. In order to achieve a temporal control over the synthesis and maintain it exclusively inside the droplets, we used a Y substrate with photocleavable protecting group on the side chain (Figure 1). This system allows the control and confinement of tyrosine enzymatic oxidation, resulting in synthetic melanin material that can be readily applied in skincare applications.

RESULTS AND DISCUSSION

We utilized the PEG/Dex ATPS system to spatially control melanin synthesis by compartmentalization and sequestration of Y and tyrosinase (Figure 1a). To temporally control the enzymatic oxidation of Y into synthetic melanin, we used side chain protected Y with the photocleavable group *o*-nitrobenzyl (ONB), which is cleaved upon UV irradiation at 365 nm, allowing Y oxidation by tyrosinase (Figure 1b). We first analyzed ONB cleavage following UV irradiation by HPLC. This analysis shows that >90% of the ONB-Y is cleaved after 180 min of UV irradiation (Supporting Information (SI) Figure S1).

To sequester tyrosinase within liquid droplets, PEG/Dex ATPS was obtained by dissolving PEG and Dex in ONB-Y or Y solution, and collecting the upper PEG-rich phase containing Dex-rich droplets, which were previously shown to efficiently sequester various proteins and enzymes.[24,27] Dex droplets were formed directly upon ATPS preparation, dispersed in the continuous PEG-rich phase. Notably, in the absence of PEG no droplets are formed by a dilute Dex solution. Tyrosinase (0.35 mg/mL) was added directly to the PEG-rich phase. The reaction was UV irradiated for 120 min as no significant difference was observed between 120 and 180 min of irradiation (SI Figure S2) and analyzed by various spectroscopy and microscopy techniques. Following ONB cleavage and oxidation ($(ONB\text{-}Y)_{cl\text{-}ox}$) in the droplets, an evident color change to dark brown was observed (SI Figure S3). We analyzed the liquid droplets before and after melanin synthesis by using transmission electron (TEM) and optical microscopy. While TEM analysis is performed on dehydrated droplets and may not fully represent the solution state, the dehydration and fixation of the droplets using negative stain allows the retention of the droplets at a stationary state and prevent their coalescence, thus enabling the detection of nanometer-sized droplets that could not be detected otherwise. The microscopy analyses show that droplet diameter ranges wildly from 200 nm (SI Figure S4) up to 150 μm after oxidation due to coalescence (SI Figure S5).

Next, we analyzed the partitioning of reactants and tyrosinase in the PEG phase compared to the Dex-rich phase by absorbance measurements of the two ATPS phases following centrifugation (see the Experimental Section). The partitioning coefficient (K) of ONB-Y and Y was found 1.22 ± 0.02 and 1.03 ± 0.03, respectively, indicating that these substrates partition within both the PEG and Dex phase with

https://doi.org/10.1021/acsami.1c21006
ACS Appl. Mater. Interfaces 2022, 14, 20520−20527

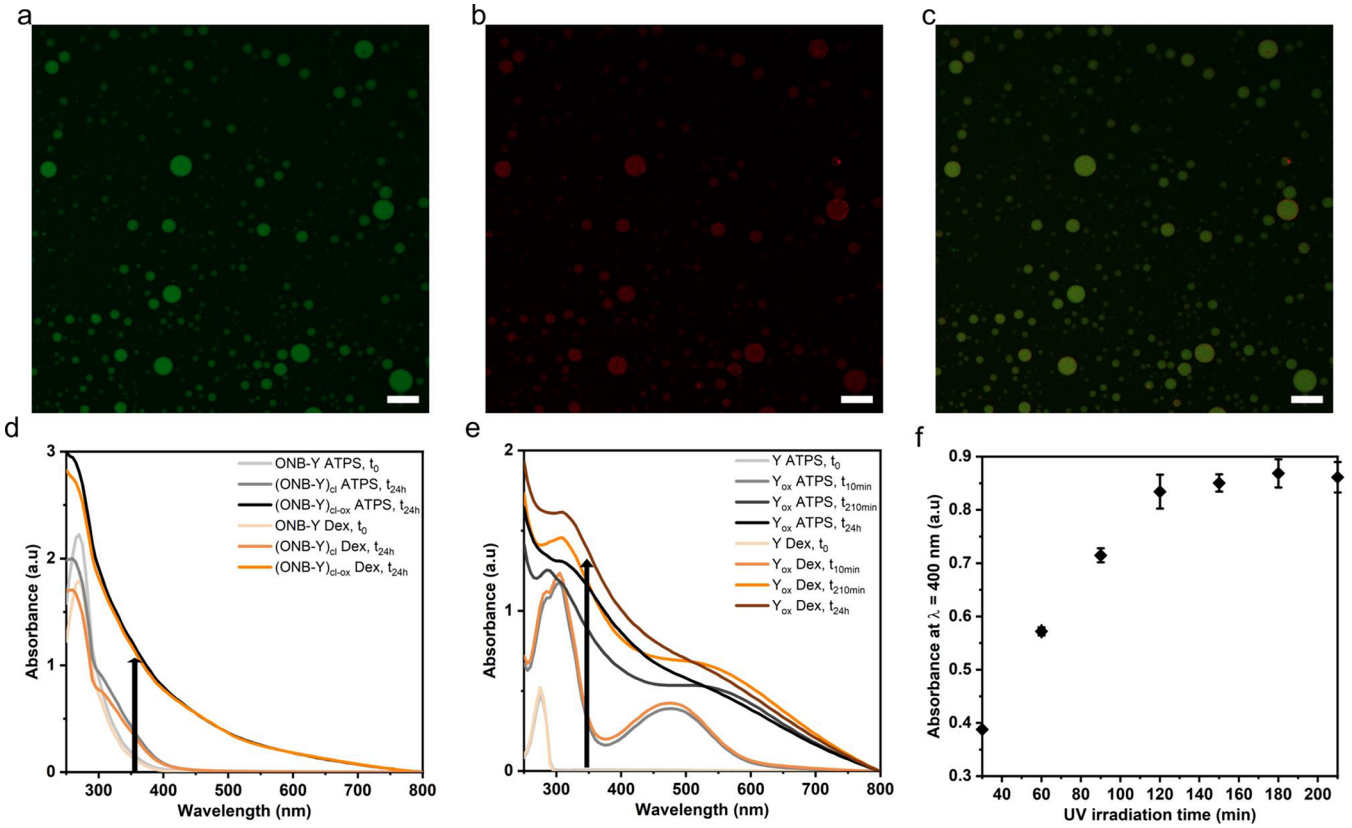

Figure 2. Characterization of tyrosinase partitioning and resulting melanin in Dex-rich droplets and bulk solutions. a–c. Confocal microscopy images of (a) FITC-labeled Dex (λ_{ex} = 488 nm), (b) Alexa 633-labeled tyrosinase (λ_{ex} = 640 nm) partitioning in Dex-rich droplets, and (c) merged image of labeled tyrosinase within labeled Dex-rich droplets. Scale bars = 50 μm. d,e. UV–vis absorbance spectra of ONB-Y (d) and Y (e) before and after oxidation in either Dex-rich droplets (ATPS) or homogeneous Dex. t_0 is the time before UV irradiation (total irradiation time was 2 h); t_{24h} is the total oxidation time. f. Absorbance intensity (λ = 400 nm) of 1 mM $(ONB\text{-}Y)_{cl\text{-}ox}$ as a function of UV irradiation time (λ = 365 nm) after 24 h of oxidation in Dex-rich droplets.

no specific preference (SI Figure S6). In contrast, tyrosinase concentration within the Dex-rich droplets phase was found 1.8-fold higher than that in the PEG phase with $K = 0.56 \pm 0.01$, indicating a preference for partitioning in the Dex phase due to its relatively higher polarity compared to PEG (SI Figure S6). To gain insights into the sequestration of tyrosinase by the Dex-rich droplets, we used real time confocal microscopy analysis. Droplets were made using 0.02% FITC-labeled Dex, and tyrosinase was labeled with Alexa Fluor 633. As shown in Figure 2a, the droplets fluoresce intensely upon excitation at λ_{ex} = 488 nm as a result of the FITC-labeled Dex, confirming that they are indeed Dex-rich, where PEG is found in the continuous phase. In addition, the droplets clearly fluoresce upon excitation at λ_{ex} = 640 nm (Figure 2b,c), indicating that the labeled tyrosinase partitions in the Dex-rich droplets. Quantitative analysis of the droplets' fluorescence shows a 8.9-fold increase in tyrosinase uptake by the Dex-rich droplets compared to the PEG phase (SI Figure S7). A similar value was previously reported for urease uptake by Dex droplets in a PEG/Dex ATPS.[27]

To analyze the optical properties of the melanin formed in the microdroplets, we performed a UV–vis spectroscopy analysis of ONB-Y and Y oxidation in droplets (ATPS) compared with reaction in homogeneous Dex. The λ_{max} of ONB-Y shifted from 269 to 260 nm following cleavage of the protecting group ($(ONB\text{-}Y)_{cl}$) (Figure 2d). The UV–vis spectra of the cleaved and oxidized ONB-Y ($(ONB\text{-}Y)_{cl\text{-}ox}$) shows intense absorption in the UVB-UVA (280–400 nm) region and broadening in the visible range (400–750 nm) at t_{24h} of oxidation, typical for eumelanin[28] and melanin-like materials.[6,7] To examine the contribution of irradiation to the UV–vis absorbance by photooxidation,[29] we performed UV–vis spectroscopy and LC–MS analyses of ONB-Y and Y following UV irradiation (20 h) in the absence of tyrosinase. As expected, no change in the absorbance or chromatogram of Y following irradiation was observed (SI Figure S8a,b), indicating that Y is not photo-oxidized. The UV–vis absorbance spectrum of $(ONB\text{-}Y)_{cl}$ does not show any indication for photooxidation (SI Figure S8a). Yet, new signals appear in the chromatogram of ONB-Y following irradiation, while those of *o*-nitrosobenzaldehyde and Y are not observed (SI Figure S8c), suggesting that these new peaks represent degradation/polymerization products of *o*-nitrosobenzaldehyde due to its high reactivity.[30,31] These results, together with previous reports which show that melanin polymerizes with small molecules,[32,33] suggest the contribution of *o*-nitrosobenzaldehyde to the UV–vis absorbance of $(ONB\text{-}Y)_{cl\text{-}ox}$, either by self-polymerization or by polymerization with the oxidized Y. No significant difference was observed between the absorbance of the $(ONB\text{-}Y)_{cl\text{-}ox}$ product formed in ATPS compared to homogeneous Dex (Figure 2d). In contrast, higher absorbance intensity was observed for melanin formed by oxidation of unprotected Y (Y_{ox}) in homogeneous Dex compared to ATPS at t_{24h} (Figure 2e).

https://doi.org/10.1021/acsami.1c21006
ACS Appl. Mater. Interfaces 2022, 14, 20520–20527

Monitoring the UV−vis absorbance of the two reactions shows the emergence of λ_{max} = 300 nm peak, attributed to dopachrome formation.[34] At $t_{3.5h}$, this absorbance peak redshifts in the Y_{ox} Dex reaction and has higher intensity compared to Y_{ox} ATPS. At t_{24h}, the two reaction mixtures absorb broadly across the UV and visible light. The chemical environment of the reaction and the distribution of the resulting melanin polymers in bulk Dex vs ATPS droplets may influence the different absorption intensity observed, as was previously shown for oxidative polymerization of 5,6-dihydroxyindole (DHI).[35] Similar results were observed for $(ONB\text{-}Y)_{cl\text{-}ox}$ and Y_{ox} in bulk phosphate buffer at pH 8 (SI Figure S9). The UV−vis absorbance of melanin formed by enzymatic oxidation of dopamine (DA_{ox}) in droplets or homogeneous Dex, or *Sepia* melanin in Dex shows typical monotonic broad absorption between 250 nm and 800 nm (SI Figure S10). Macroscopic images of the DA_{ox} melanin materials formed in droplets compared to homogeneous Dex show higher solubility of the reaction mixture in droplets, where reaction in bulk Dex resulted in formation of black precipitation (SI Figure S11c). A similar trend was observed following spontaneous oxidation of DA (10 mM) in droplets compared to bulk Dex (SI Figure S11d). Previous reports show that water-soluble polymers can help improving the colloidal stability of synthetic melanin or melanin-TiO_2.[36] While this approach also results in water-soluble melanin, it is fundamentally different from the system presented here, which relies on compartmentalization of melanin synthesis and accumulation of the melanin product in liquid droplets. Next, we evaluated how varying the irradiation time, and in turn ONB-Y cleavage, influence the formation of melanin product in the droplets. Droplets containing tyrosinase and ONB-Y were irradiated for varying periods of time, and the UV−vis absorbance spectra were acquired after 24 h of oxidation. This analysis shows a direct correlation between the irradiation time of the droplets and the increase in intensity and broadening of the absorbance (SI Figure S12, Figure 2f), demonstrating that melanin formation can be temporally controlled by tuning the irradiation time.

To get insights into the difference in the UV−vis absorption of the melanin formed by Y_{ox} in droplets compared to bulk and to analyze whether this difference is a result of altered conversion rate, we performed LC-MS/MS analysis of Y_{ox} reaction mixture in droplets (ATPS) or homogeneous Dex (SI Figures S13 and S14). Since the melanin product typically consist multiple masses, we monitored Y depletion following enzymatic oxidation (SI Figure S13a,b). We first developed a method to identify Y in the ATPS mixture or in homogeneous Dex. Mass spectral parameters were optimized for Y by varying ion source parameters for scan mode and collision energy for product ion mode (MS/MS). Significant fragment signals in the mass spectrum were analyzed. Extracted ion chromatograms (EIC) of Y and its major fragments (SI Figure S13c) shows a complete disappearance of Y after 24 h of oxidation in both ATPS and homogeneous Dex (SI Figure S13a,b). Thus, the difference in UV−vis absorbance intensity of the Y_{ox} melanin in droplets compared to the bulk is not a result of reduced catalysis in droplets. Analyzing the polymeric species formed by Y_{ox} in homogeneous Dex revealed the formation of several signals which emerge upon oxidation for 24 h and are not present in sample of unoxidized Y. These signals represent high molecular weight (MW) polymers with masses of 13 kDa, 21 kDa, and 41 kDa, alongside low MW species with a mass of 2−5 kDa (SI Figure S14a1−a3). The polymeric species formed by Y_{ox} in droplets could not be convoluted from the intense signal of PEG, which is found in high concentration in the ATPS (SI Figure S13b). Notably, the presence of Dex in the reaction mixture might increase the solubility of the high MW melanin polymers, and in turn, these could be analyzed using LC−MS. To get a better understanding of the polymeric species' composition, we analyzed the initial oxidation products of Y_{ox} by high-resolution LC−MS (SI Figure S15). This analysis shows a decrease of the Y signal (SI Figure S15a) alongside formation of new species (SI Figure S15b) with a mass of 194.043 m/z, which according to mass calculations fits to the addition of a single oxygen and reduction of four hydrogens from the molecular formula of Y. These chemical changes correspond to the formation of either 5,6-dioxo-indole-2-carboxylic acid (dopachrome) or 5,6-dihydroxy-1H-indole-2-carboxylic acid (DHIC), as described in the Raper−Mason pathway[37] (SI Figure S15b). The emergence of this species at short oxidation time indicates that the high MW polymers observed at 24 h of oxidation (SI Figure S14) most likely represent melanin polymers.

Next, we utilized melanin's intrinsic fluorescence to monitor product formation within droplets by using confocal microscopy, which allows for a spatial resolution analysis of liquid samples. While the fluorescent signal of $(ONB\text{-}Y)_{cl\text{-}ox}$ was too weak to be monitored by confocal microscopy (SI Figure S16), the droplets containing Y_{ox} fluoresced after 24 h of oxidation at λ_{ex} = 405 nm as a result of melanin formation (Figure 3a). The fluorescence intensity of Y_{ox} melanin within

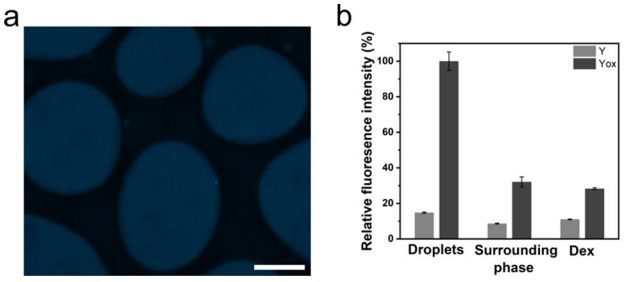

Figure 3. Confocal microscopy analysis of the intrinsic fluorescence of Y_{ox} melanin. (a) Confocal microscopy image of Y_{ox} melanin formed inside droplets. Scale bar = 20 μm. (b) analysis of the intrinsic fluorescence of Y_{ox} melanin formed inside droplets, at the surrounding phase, or in homogeneous Dex. Fluorescence was measured at λ_{ex} = 405 nm, values represent average of relative intensity, n = 27 for droplets or surrounding phase and n = 18 for Dex.

droplets was <3-fold higher than that in the surrounding phase (Figure 3b), indicating that the melanin product is accumulated and compartmentalized within the droplets. This compartmentalization provides a means to control and regulate melanin reactivity in complex mixtures. Similarly, one of the functionalities attributed to melanosomes is the compartmentalization and storage of melanin to prevent the reaction of the pigment with cellular biomolecules, which might have a pathological outcome.[3]

Lastly, we chemically analyzed the resulting melanin material in the droplets at a spatial resolution by using time-of-flight secondary ion mass spectrometry (ToF-SIMS). While this analysis is performed in the dried state, which is likely different from the solution state, it provides identification and mapping of molecules and chemical structures at high spatial

https://doi.org/10.1021/acsami.1c21006
ACS Appl. Mater. Interfaces 2022, 14, 20520−20527

resolution.[38,39] The biosynthesis of the brown/black eumelanin involves oxidation of tyrosine into 3,4-dihydroxyphenylalanine (DOPA) and then to dopaquinone followed by spontaneous cyclization to cycloDOPA, which is rapidly oxidized to dopachrome and DOPA,[40] and eventually polymerization and stacking of DHI and DHIC to eumelanin (SI Figure S17). Masses of ions that were previously reported as characteristic for eumelanin, including C_3N^-, C_3NO^-, and C_5N^-,[38,39] could be detected only in bulk oxidation reactions, presumably due to interference of signal from ions of the PEG/Dex system. Yet, these masses are not indicative for Y oxidation-polymerization as they also appear in samples of unoxidized ONB-Y before and after cleavage (SI Figure S18), suggesting a similar fragmentation pattern of the ONB group and the oxidized species. Depth profiling of the droplets using sputtering of the samples' surface shows an increase in the intensity of CN^- ions inside droplets containing either $(ONB\text{-}Y)_{cl\text{-}ox}$ or Y_{ox} (Figure 4). This analysis suggests that the increase

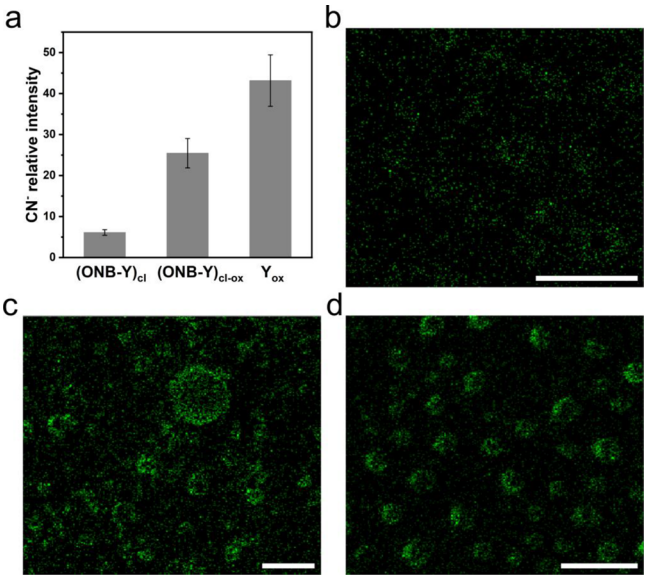

Figure 4. ToF-SIMS analysis of 1 mM $(ONB\text{-}Y)_{cl}$, $(ONB\text{-}Y)_{cl\text{-}ox}$ and Y_{ox} at t_{24h} in Dex-rich droplets. (a) Relative intensity of CN^- ion of $(ONB\text{-}Y)_{cl}$, $(ONB\text{-}Y)_{cl\text{-}ox}$ and Y_{ox}. Samples were analyzed to obtain the normalized CN^- ions intensity (normalized to O^- ions) for droplets obtained in the three samples. b–d. Chemical ion maps of CN^- ions taken after sputtering of (b) $(ONB\text{-}Y)_{cl}$, (c) $(ONB\text{-}Y)_{cl\text{-}ox}$, and (d) Y_{ox}. Scale bars = 10 μm.

in CN^- ions observed following oxidation for both $(ONB\text{-}Y)_{cl\text{-}ox}$ and Y_{ox} is due to formation of new bonds during the oxidation-polymerization process and that the reaction mainly occurs inside the droplets. These results correlate with the confocal microscopy analysis in solution (Figure 3) showing the melanin product in the droplets. The higher intensity of CN^- ions and fluorescence in Y_{ox} samples might be related to the increased accessibility of the free Y for tyrosinase oxidation compared to that of ONB-Y.

CONCLUSIONS

Our findings indicate that tyrosinase sequestration by the Dex-rich droplets allows for confined local reactivity, resulting in formation of soluble melanin in the compartments. Similar findings were shown by others, where locally higher concentration of the enzyme urease inside the Dex-rich phase restricts $CaCO_3$ formation reaction exclusively inside this phase.[27] Accumulation and compartmentalization of the melanin product in the droplets offers a tool to regulate the reactivity of the product. In summary, we have successfully designed a system for the spatiotemporal control of melanin synthesis. While most synthetic mimics of melanin composed of insoluble materials, the current system utilizes aqueous compartments to generate a water-soluble melanin. Due to the biocompatibility of its components and the photoprotective properties of the resulting material, this system has a tremendous technological potential in sun protection applications and can be readily formulated in skincare products. Moreover, this work suggests that the current method can be further developed to control the synthesis of additional insoluble biopolymers for various biotechnological applications.

EXPERIMENTAL SECTION

Materials. *o*-(2-Nitrobenzyl)-L-tyrosine hydrochloride, sodium phosphate monobasic, and sodium phosphate dibasic were purchased from Holland Moran. Thermo Fisher Scientific Alexa Fluor 633 Protein Labeling Kit was purchased from Rhenium. PEG 8 kDa, dextran 10 kDa, fluorescein isothiocyanate (FITC)-Dex 10 kDa conjugate, L-tyrosine and tyrosinase (isolated from *Agaricus bisporus*) were purchased from Sigma-Aldrich. Water, acetonitrile, and trifluoroacetic acid (HPLC grade) were purchased from Bio-Lab.

ONB-Y and Y Sample Preparation. ONB-Y stock solution was prepared by dissolving ONB-Y in DMSO (2%) and 50 mM (or 5 mM) phosphate buffer at pH 8 and sonicating for 4–8 h, followed by filtration. The same procedure was used for preparation of Y stock solution.

Formation of PEG/Dex ATPS. ATPS composition was based on previous studies.[26] ATPS stocks were prepared at 10 w/w% 8 kDa PEG and 16 w/w% 10 kDa Dex. PEG/Dex were dissolved in 1 mM ONB-Y stock solution (or in 50 mM phosphate buffer at pH 8). Buffer was manually prepared in-house using a combination of sodium phosphate monobasic and sodium phosphate dibasic. ATPS was centrifuged to separate the two phases, and then the upper PEG-rich phase was removed via pipet. The same procedure was used for L-tyrosine (Y). Homogeneous Dex solution was prepared by dissolving 16 w/w% 10 kDa Dex in a substrate stock solution, or in 50 mM phosphate buffer.

ONB-Y Cleavage Kinetics. ONB-Y was dissolved to 1.3 mM in double distilled water (ddw). The sample was irradiated in a UV box (λ = 365 nm, 6 W) for 180 min. Samples were taken for HPLC analysis every 15 min. Samples were analyzed using analytical high-performance liquid chromatography (HPLC) on a Dionex SD Ultimate 3000 UHPLC standard system equipped with a diode-array detection (DAD) Detector. Mobile phases were (A) H_2O (0.1% TFA) and (B) MeCN (0.1% TFA). Separation conditions for all the samples were as follows: Analytical Hypersil GOLD RP-C18 Column (from Thermo Fisher) 175 Å 1.9 μm 50 × 2.1 mm with a flow rate of 0.6 mL/min. Gradient was as follows: H_2O/MeCN 0 min (90/10), 0–2.500 min (45/55), 2.500–3.000 min (10/90), 3.000–3.250 min (10/90), 3.250–5.000 min (90/10). Samples were analyzed at λ = 214 nm.

Tyrosine Oxidation in Droplets. Tyrosinase was dissolved at 3.5 mg/mL in 50 mM phosphate buffer at pH 8 and diluted 10-fold in the Dex-rich droplets solution (final concentration of 0.35 mg/mL). The sample was transferred into 96 multiwell plate and irradiated (λ = 365 nm, 6 W) in a UV-box for 2 h.

Tyrosine Oxidation in Bulk. Tyrosinase was dissolved at 3.5 mg/mL in 50 mM (or 5 mM) phosphate buffer at pH 8 and diluted 10-fold in each sample (final concentration of 0.35 mg/mL). The sample was transferred into a 96 multiwell plate and irradiated (λ = 365 nm, 6 W) in a UV-box for 2 h. After irradiation, the sample was analyzed every few hours by UV–vis absorbance measurements and imaged by

https://doi.org/10.1021/acsami.1c21006
ACS Appl. Mater. Interfaces 2022, 14, 20520–20527

confocal microscopy (150 μL sample) and transmission electron microscopy.

UV−vis Absorbance Measurements. UV−vis absorbance spectra of solution samples containing oxidized ONB-Y, Y, or DA in ATPS and homogeneous Dex were taken using Synergy H1 microplate reader, between 230 and 800 nm (every 5 nm), after 30 s of shaking before each measurement. DA_{ox} was prepared by dissolving 1 mM DA in DMSO (2%) and 50 mM phosphate buffer at pH 8, then tyrosinase was dissolved at 3.5 mg/mL in 50 mM phosphate buffer at pH 8 and diluted 10-fold in the (final concentration of 0.35 mg/mL). *Sepia* melanin solution was prepared by dissolving 0.6 mg/mL of *Sepia officinalis* melanin (Sigma) in 1 M NaOH with 4% DMSO. After 10 h of bath sonication the solution was diluted by 50% v/v% 100 mM phosphate buffer. The pH was adjusted to a value of 10 by adding 1 M HCl solution and then 100 mM phosphate buffer to receive a final *Sepia* melanin concentration of 0.18 mg/mL (equivalent to the concentration of Y in the oxidation experiments). Control samples for each medium were considered as background, and their absorbance data were subtracted from the data of each sample (control and unoxidized samples were not diluted).

Confocal Microscopy Analysis. Samples were directly imaged from a multiwell plate, using a ZEISS LSM 900 inverted confocal microscopy with 10× or x20/0.8 NA Plan-Apochromat objective. Images were collected and processed using Zen software (Zeiss). Bright field images were obtained by PMT channel. Fluorescence images were taken using 640 and 488 nm lasers (for Alexa Fluor 633 and FITC, respectively).

Confocal Microscopy Analysis of Tyrosinase Sequestration. Labeling: Tyrosinase was labeled at amines using succinimidyl ester functionalized Alexa Fluor 633 labeling kit (Invitrogen). The labeled enzyme was purified using a gel filtration column. Partitioning: labeled tyrosinase was diluted 1:5 (final concentration of 0.09 mg/mL) in an ATPS prepared with FITC-Dex. ATPS were prepared with 0.02% FITC-Dex, 10 w/w% PEG 8 kDa and 15.98 w/w% Dex 10 kDa ATPS in 50 mM phosphate buffer at pH 8. After 18 h of incubation, 40 μL of the sample was transferred into an imaging multiwell plate. The fluorescence intensity was averaged from 12 μm circles, 48 droplets, and 48 background points were analyzed to obtain a fluorescence intensity profile to evaluate tyrosinase partitioning in the Dex-rich droplets. Tyrosinase uptake by the Dex-rich droplets was calculated from the average fluorescence intensity values of Alexa Fluor 633 as described in eq 1.

$$\text{tyrosinase uptak} = \frac{\text{fluoresence intensity inside the droplets}}{\text{fluoresence intensity at the background}} \quad (1)$$

Partitioning of Y, ONB-Y, and Tyrosinase in ATPS. Y: Absorbance measurements of different Y concentration in 2% DMSO in 50 mM phosphate buffer have been performed to obtain a calibration curve (λ = 275 nm). Partitioning evaluation of 1 mM Y solution was performed by dissolving 10 w/w% 8 kDa PEG and 16 w/w% 10 kDa Dex in 1 mM Y. The ATPS was centrifuged and each phase was collected, and centrifuged again (repeated twice for each phase). The concentration of Y in each phase was calculated after subtraction of the background (PEG or Dex separated in the same manner, which were dissolved in 2% DMSO in 50 mM phosphate buffer) of each sample. ONB-Y: The same procedure was used for ONB-Y, with the exception of using lower concentrations for the calibration curve measurements (due to high absorbance values, λ = 269 nm), and 0.4 mM ONB-Y solution was used for the partitioning experiment. Tyrosinase: For the calibration curve (λ = 280 nm), different tyrosinase concentrations were prepared in 50 mM phosphate buffer, and diluted 10-fold in each phase separately (ATPS dissolved in 2% DMSO in 50 mM phosphate buffer, separated as described for Y). Absorbance measurements and background subtraction was done as described for Y. Partitioning evaluation was performed by dissolving 5 mg/mL tyrosinase in 50 mM phosphate buffer and diluted 10-fold in ATPS dissolved in 2% DMSO in 50 mM phosphate buffer (final concentration of 0.5 mg/mL). The ATPS was mixed by rotation for 2 h. Then the phases were separated as described for Y, and concentration in each phase was determined. All partitioning coefficients, K, were calculated from the average concentrations of each phase as described in eq 2.

$$K = \frac{C_{PEG}}{C_{Dex}} \quad (2)$$

Transmission Electron Microscopy. Ten μL of the sample solution were applied to a carbon-coated grid and incubated for 2 min. Excess solution was removed by blotting the grid with a piece of filter paper, followed by staining with 10 μL of 2% (w/v) uranyl acetate solution for 2 min. After blotting excess stain solution, the grid was left to air-dry. The negatively stained sample was imaged in a JEM-1400Plus TEM operating at 80 kV. Images were recorded using SIS Megaview III camera, iTEM the Tem imaging platform (Olympus).

Liquid Chromatography−Mass Spectrometry (LC−MS) Analysis of Tyrosine Oxidation. Unoxidized samples were diluted (10% dilution with 50 mM phosphate buffer). The samples were taken directly from the 96 multiwell plate. All the equipment for the analyses was from Agilent technologies and consisted of a 6545 QTOF mass spectrometer which was equipped with an electrospray ionization interface (ESI) coupled to a 1260 UHPLC, a G4204A quaternary pump, G4226A ALS autosampler, and G1316C thermostated column compartment. UHPLC was carried out on a ZORBAX RRHD Eclipse Plus C18, 95 Å, 2.1 × 50 mm, 1.8 μm column, with water (0.1% formic acid)-MeCN gradient elution, from 5 to 95% acetonitrile for 10 min at a flow rate of 0.5 mL/min. Ten μL of each sample were injected into the LC-MS/MS instrument in triplicates and an average peak area of three analyses was calculated. The water−acetonitrile solution was injected as a blank within a sequence of samples to confirm that there was no cumulative carryover. Ion source parameters for tyrosine detection were as follow: temperature was set to 300 °C, Fragmentor 100 V and ion spray voltage was 3.5 kV and for melanin: temperature was set to 300 °C, Fragmentor 250 V and ion spray voltage was 4.5 kV, nozzle voltage 1500 V.

Quantification of Tyrosine Oxidation Using Confocal Microscopy. Unoxidized samples were diluted (10% dilution with 50 mM phosphate buffer). Samples containing 1 mM Y or Y_{ox} were directly imaged from a multiwell plate using a ZEISS LSM 900 inverted confocal microscopy with 405 nm laser. Images were collected and processed using the Zen software (Zeiss). The histograms were stretched from the lower 30% of the original histogram. The fluorescence intensity was averaged from 30 μm circles. The number of sampled droplets and spots outside the droplets (in the surrounding phase) is n = 27 for the ATPS samples and n = 18 for the homogeneous Dex samples. Values were normalized to percentage.

Time-of-Flight Secondary Ion Mass Spectrometry. The sample was diluted 10-fold in ddw. Ten μL of the diluted sample were applied to a silicon chip and left air-dried in a desiccator overnight. ToF-SIMS data acquisition was performed using a TRIFT II instrument (Physical Electronics, U.S.). For high mass resolution spectroscopy, the instrument employed a 15 keV Ga^+ ion source. The 600 pA dc primary ion beam was pulsed at 10 kHz frequency with a pulse width of 15 ns. During high spatial resolution imaging, the instrument employed the Ga^+ source at 25 keV, 60 pA dc current and 30 ns pulses. A low-energy electron beam was used for charge compensation. For sputtering purposes, a 500 eV Cs^+ ion gun with 50 nA current was used. The sputtering was applied in order to see a possible melanin content inside the polymer droplets. Negative ions of CN^- were diagnostic for melanin inside the polymer droplets and used to image the melanin distribution. For the droplets without melanin, the CN^- ions intensity was low and similar to the surrounding area, while the droplets with melanin were highlighted with the CN^- ions. Negative ions of O^- and CHO_2^- were representative for the PEG and Dex polymers, significantly highlighting the droplets on ion images. Both these ions were used for normalization of CN^- signal to compare between samples and show similar results. In order to exclude impact of CN^- background

https://doi.org/10.1021/acsami.1c21006
ACS Appl. Mater. Interfaces 2022, 14, 20520−20527

between the droplets, a retrospective data analysis was applied. During acquisition of mass spectra and images, all data were saved in RAW data files, so that after finishing the analysis, it was possible to use a "region of interest" option. Inside the whole analysis area, the droplets only areas were specified, and mass spectra were extracted from the droplets only. Three areas of each sample were analyzed. In order to compare between the different analyzed samples in 5 mM phosphate buffer, the intensity of the relevant peaks was normalized by total counts. Three or four areas of each sample were analyzed.

■ ASSOCIATED CONTENT

Supporting Information

The Supporting Information is available free of charge at https://pubs.acs.org/doi/10.1021/acsami.1c21006.

HPLC analysis of ONB-Y cleavage; UV−vis spectroscopy analysis of melanin in droplets; macroscopic images, confocal microscopy images, and TEM micrographs of melanin in PEG/Dex droplets; ToF-SIMS analysis of the melanin formed in droplets (PDF)

■ AUTHOR INFORMATION

Corresponding Author

Ayala Lampel − *Shmunis School of Biomedicine and Cancer Research, George S. Wise Faculty of Life Sciences, Tel Aviv University, Tel Aviv 69978, Israel; Center for Nanoscience and Nanotechnology, Tel Aviv University, Tel Aviv 69978, Israel; Sagol Center for Regenerative Biotechnology, Tel Aviv University, Tel Aviv 69978, Israel; Center for the Physics and Chemistry of Living Systems, Tel Aviv University, Tel Aviv 69978, Israel;* orcid.org/0000-0003-2733-9197; Email: ayalalampel@tauex.tau.ac.il

Authors

Tlalit Massarano − *Shmunis School of Biomedicine and Cancer Research, George S. Wise Faculty of Life Sciences, Tel Aviv University, Tel Aviv 69978, Israel*

Avigail Baruch Leshem − *Shmunis School of Biomedicine and Cancer Research, George S. Wise Faculty of Life Sciences, Tel Aviv University, Tel Aviv 69978, Israel*

Michal Weitman − *Department of Chemistry, Bar -Ilan University, Ramat-Gan 5290002, Israel*

Complete contact information is available at: https://pubs.acs.org/10.1021/acsami.1c21006

Author Contributions

T.M and A.L conceived and designed the analyses, and wrote the manuscript. T.M collected and analyzed the data. Confocal microscopy analyses of melanin fluorescence were performed by A.B.L. LC-MS/MS experiments and analyses were performed by M.W.

Funding

This research was supported by the ISRAEL SCIENCE FOUNDATION (Grant No. 2589/21). T.M thanks the ADAMA Center for Novel Delivery Systems in Crop Protection for the PhD ADAMA Fellowship and the Marian Gertner Institute for Medical Nanosystems for the Gertner Scholarship.

Notes

The authors declare no competing financial interest.

■ ACKNOWLEDGMENTS

We thank Dr. A. Gladkikh for the help with ToF-SIMS analysis, Dr. V. Holdengreber for the help with the TEM imaging, Dr. M. Gal and Dr. I. Sher for the help with enzyme purification, and the Chaoul Center for Nanoscale Systems of Tel Aviv University for the use of instruments and staff assistance.

■ REFERENCES

(1) Banani, S. F.; Lee, H. O.; Hyman, A. A.; Rosen, M. K. Biomolecular Condensates: Organizers of Cellular Biochemistry. *Nat. Rev. Mol. Cell Biol.* **2017**, *18* (5), 285−298.

(2) D'Alba, L.; Shawkey, M. D. Melanosomes: Biogenesis, Properties, and Evolution of an Ancient Organelle. *Physiol. Rev.* **2019**, *99* (1), 1−19.

(3) Raposo, G.; Marks, M. S. Melanosomes - Dark Organelles Enlighten Endosomal Membrane Transport. *Nat. Rev. Mol. Cell Biol.* **2007**, *8* (10), 786−797.

(4) Liu, B. W.; Huang, P. C.; Li, J. F.; Wu, F. Y. Colorimetric Detection of Tyrosinase during the Synthesis of Kojic Acid/Silver Nanoparticles under Illumination. *Sensors Actuators, B Chem.* **2017**, *251*, 836−841.

(5) McGlinchey, R. P.; Shewmaker, F.; McPhie, P.; Monterroso, B.; Thurber, K.; Wickner, R. B. The Repeat Domain of the Melanosome Fibril Protein Pmel17 Forms the Amyloid Core Promoting Melanin Synthesis. *Proc. Natl. Acad. Sci. U. S. A* **2009**, *106* (33), 13731−13736.

(6) Lampel, A.; McPhee, S. A.; Park, H. A.; Scott, G. G.; Humagain, S.; Hekstra, D. R.; Yoo, B.; Frederix, P. W. J. M.; Li, T. De; Abzalimov, R. R.; Greenbaum, S. G.; Tuttle, T.; Hu, C.; Bettinger, C. J.; Ulijn, R. V. Polymeric Peptide Pigments with Sequence-Encoded Properties. *Science* **2017**, *356* (6342), 1064−1068.

(7) Reddy, S. M. M.; Raßlenberg, E.; Sloan-Dennison, S.; Hesketh, T.; Silberbush, O.; Tuttle, T.; Smith, E.; Graham, D.; Faulds, K.; Ulijn, R. V.; Ashkenasy, N.; Lampel, A. Proton-Conductive Melanin-Like Fibers through Enzymatic Oxidation of a Self-Assembling Peptide. *Adv. Mater.* **2020**, *2003511* (32), 1−7.

(8) Lampel, A.; McPhee, S. A.; Kassem, S.; Sementa, D.; Massarano, T.; Aramini, J. M.; He, Y.; Ulijn, R. V. Melanin-Inspired Chromophoric Microparticles Composed of Polymeric Peptide Pigments. *Angew. Chemie Int. Ed.* **2021**, *60* (14), 7564−7569.

(9) Xiao, M.; Li, Y.; Allen, M. C.; Deheyn, D. D.; Yue, X.; Zhao, J.; Gianneschi, N. C.; Shawkey, M. D.; Dhinojwala, A. Bio-Inspired Structural Colors Produced via Self-Assembly of Synthetic Melanin Nanoparticles. *ACS Nano* **2015**, *9* (5), 5454−5460.

(10) Xiao, M.; Li, Y.; Zhao, J.; Wang, Z.; Gao, M.; Gianneschi, N. C.; Dhinojwala, A.; Shawkey, M. D. Stimuli-Responsive Structurally Colored Films from Bioinspired Synthetic Melanin Nanoparticles. *Chem. Mater.* **2016**, *28* (15), 5516−5521.

(11) Xiao, M.; Hu, Z.; Wang, Z.; Li, Y.; Tormo, A. D.; Le Thomas, N.; Wang, B.; Gianneschi, N. C.; Shawkey, M. D.; Dhinojwala, A. Bioinspired Bright Noniridescent Photonic Melanin Supraballs. *Sci. Adv.* **2017**, *3* (9), 1−8.

(12) Ju, K. Y.; Lee, Y.; Lee, S.; Park, S. B.; Lee, J. K. Bioinspired Polymerization of Dopamine to Generate Melanin-like Nanoparticles Having an Excellent Free-Radical-Scavenging Property. *Biomacromolecules* **2011**, *12* (3), 625−632.

(13) Wang, C.; Wang, D.; Dai, T.; Xu, P.; Wu, P.; Zou, Y.; Yang, P.; Hu, J.; Li, Y.; Cheng, Y. Skin Pigmentation-Inspired Polydopamine Sunscreens. *Adv. Funct. Mater.* **2018**, *28* (33), 1−9.

(14) Huang, Y.; Li, Y.; Hu, Z.; Yue, X.; Proetto, M. T.; Jones, Y.; Gianneschi, N. C. Mimicking Melanosomes: Polydopamine Nanoparticles as Artificial Microparasols. *ACS Cent. Sci.* **2017**, *3* (6), 564−569.

(15) Xiao, M.; Shawkey, M. D.; Dhinojwala, A. Bioinspired Melanin-Based Optically Active Materials. *Adv. Opt. Mater.* **2020**, *8* (19), 1−15.

(16) Cavallini, C.; Vitiello, G.; Adinolfi, B.; Silvestri, B.; Armanetti, P.; Manini, P.; Pezzella, A.; D'Ischia, M.; Luciani, G.; Menichetti, L. Melanin and Melanin-like Hybrid Materials in Regenerative Medicine. *Nanomaterials* **2020**, *10* (8), 1−32.

(17) Battistella, C.; Mccallum, N. C.; Gnanasekaran, K.; Zhou, X.; Caponetti, V.; Montalti, M.; Gianneschi, N. C. Mimicking Natural Human Hair Pigmentation with Synthetic Melanin. *ACS Cent. Sci.* **2020**, *6* (7), 1179−1188.
(18) Vitiello, G.; Zanfardino, A.; Tammaro, O.; Di Napoli, M.; Caso, M. F.; Pezzella, A.; Varcamonti, M.; Silvestri, B.; D'Errico, G.; Costantini, A.; Luciani, G. Bioinspired Hybrid Eumelanin-TiO2 Antimicrobial Nanostructures: The Key Role of Organo-Inorganic Frameworks in Tuning Eumelanin's Biocide Action Mechanism through Membrane Interaction. *RSC Adv.* **2018**, *8* (50), 28275−28283.
(19) Pezzella, A.; Capelli, L.; Costantini, A.; Luciani, G.; Tescione, F.; Silvestri, B.; Vitiello, G.; Branda, F. Towards the Development of a Novel Bioinspired Functional Material: Synthesis and Characterization of Hybrid TiO 2/DHICA-Melanin Nanoparticles. *Mater. Sci. Eng., C* **2013**, *33* (1), 347−355.
(20) Poinard, B.; Neo, S. Z. Y.; Yeo, E. L. L.; Heng, H. P. S.; Neoh, K. G.; Kah, J. C. Y. Polydopamine Nanoparticles Enhance Drug Release for Combined Photodynamic and Photothermal Therapy. *ACS Appl. Mater. Interfaces* **2018**, *10* (25), 21125−21136.
(21) Martin, N.; Tian, L.; Spencer, D.; Coutable-Pennarun, A.; Anderson, J. L. R.; Mann, S. Photoswitchable Phase Separation and Oligonucleotide Trafficking in DNA Coacervate Microdroplets. *Angew. Chemie - Int. Ed.* **2019**, *58* (41), 14594−14598.
(22) Capasso Palmiero, U.; Küffner, A. M.; Krumeich, F.; Faltova, L.; Arosio, P. Adaptive Chemoenzymatic Microreactors Composed of Inorganic Nanoparticles and Bioinspired Intrinsically Disordered Proteins. *Angew. Chemie - Int. Ed.* **2020**, *59* (21), 8138−8142.
(23) Sing, C. E.; Perry, S. L. Recent Progress in the Science of Complex Coacervation. *Soft Matter* **2020**, *16* (12), 2885−2914.
(24) Crowe, C. D.; Keating, C. D. Liquid−Liquid Phase Separation in Artificial Cells. *Interface Focus* **2018**, *8* (5), 20180032.
(25) Dewey, D. C.; Strulson, C. A.; Cacace, D. N.; Bevilacqua, P. C.; Keating, C. D. Bioreactor Droplets from Liposome-Stabilized All-Aqueous Emulsions. *Nat. Commun.* **2014**, *5* (1), 1−9.
(26) Strulson, C. A.; Molden, R. C.; Keating, C. D.; Bevilacqua, P. C. RNA Catalysis through Compartmentalization. *Nat. Chem.* **2012**, *4* (11), 941−946.
(27) Cacace, D. N.; Keating, C. D. Biocatalyzed Mineralization in an Aqueous Two-Phase System: Effect of Background Polymers and Enzyme Partitioning. *J. Mater. Chem. B* **2013**, *1* (13), 1794−1803.
(28) d'Ischia, M.; Napolitano, A.; Pezzella, A.; Meredith, P.; Buehler, M. Melanin Biopolymers: Tailoring Chemical Complexity for Materials Design. *Angew. Chemie - Int. Ed.* **2020**, *59* (28), 11196−11205.
(29) Maeda, K.; Hatao, M. Involvement of Photooxidation of Melanogenic Precursors in Prolonged Pigmentation Induced by Ultraviolet A. *J. Invest. Dermatol.* **2004**, *122* (2), 503−509.
(30) Givens, R. S.; Rubina, M.; Wirz, J. Applications of P-Hydroxyphenacyl (PHP) and Coumarin-4-Ylmethyl Photoremovable Protecting Groups. *Photochem. Photobiol. Sci.* **2012**, *11* (3), 472−488.
(31) Klán, P.; Šolomek, T.; Bochet, C. G.; Blanc, A.; Givens, R.; Rubina, M.; Popik, V.; Kostikov, A.; Wirz, J. Photoremovable Protecting Groups in Chemistry and Biology: Reaction Mechanisms and Efficacy. *Chem. Rev.* **2013**, *113* (1), 119−191.
(32) Ibrahim, H.; Aubry, A. F. Development of a Melanin-Based High-Performance Liquid Chromatography Stationary Phase and Its Use in the Study of Drug-Melanin Binding Interactions. *Anal. Biochem.* **1995**, *229* (2), 272−277.
(33) Soddu, G.; Sanjust, E.; Murgia, S.; Rescigno, A. Interference of Some Tryptophan Metabolites in the Formation of Melanin In Vitro. *Pigment Cell Res.* **2004**, *17* (2), 135−141.
(34) Zhu, X.; Hu, J.; Zhao, Z.; Sun, M.; Chi, X.; Wang, X.; Gao, J. Kinetic and Sensitive Analysis of Tyrosinase Activity Using Electron Transfer Complexes: In Vitro and Intracellular Study. *Small* **2015**, *11* (7), 862−870.
(35) Pezzella, A.; Ambrogi, V.; Arzillo, M.; Napolitano, A.; Carfagna, C.; D'Ischia, M. 5,6-Dihydroxyindole Oxidation in Phosphate Buffer/Polyvinyl Alcohol: A New Model System for Studies of Visible Chromophore Development in Synthetic Eumelanin Polymers. *Photochem. Photobiol.* **2010**, *86* (3), 533−537.
(36) Pota, G.; Zanfardino, A.; Di Napoli, M.; Cavasso, D.; Varcamonti, M.; D'Errico, G.; Pezzella, A.; Luciani, G.; Vitiello, G. Bioinspired Antibacterial PVA/Melanin-TiO2 Hybrid Nanoparticles: The Role of Poly-Vinyl-Alcohol on Their Self-Assembly and Biocide Activity. *Colloids Surfaces B Biointerfaces* **2021**, *202* (September 2020), 111671.
(37) Ni, Q. Z.; Sierra, B. N.; La Clair, J. J.; Burkart, M. D. Chemoenzymatic Elaboration of the Raper-Mason Pathway Unravels the Structural Diversity within Eumelanin Pigments. *Chem. Sci.* **2020**, *11* (30), 7836−7841.
(38) Lindgren, J.; Uvdal, P.; Sjövall, P.; Nilsson, D. E.; Engdahl, A.; Schultz, B. P.; Thiel, V. Molecular Preservation of the Pigment Melanin in Fossil Melanosomes. *Nat. Commun.* **2012**, *3* (1), 1−7.
(39) Lindgren, J.; Sjövall, P.; Carney, R. M.; Uvdal, P.; Gren, J. A.; Dyke, G.; Schultz, B. P.; Shawkey, M. D.; Barnes, K. R.; Polcyn, M. J. Skin Pigmentation Provides Evidence of Convergent Melanism in Extinct Marine Reptiles. *Nature* **2014**, *506* (7489), 484−488.
(40) Land, E. J.; Ito, S.; Wakamatsu, K.; Riley, P. A. Rate Constants for the First Two Chemical Steps of Eumelanogenesis. *Pigment Cell Res.* **2003**, *16* (5), 487−493.

NOTE ADDED AFTER ASAP PUBLICATION

Due to a production error, this paper was published ASAP on April 22, 2022, without the updated Supporting Information file uploaded. The corrected version was reposted on April 25, 2022.

https://doi.org/10.1021/acsami.1c21006
ACS Appl. Mater. Interfaces 2022, 14, 20520−20527